Monte Carlo study on ultrasound backscattering by three-dimensional distributions of red blood cells

Ratan K. Saha[1,*] and Guy Cloutier[1,2,†]

[1]*Laboratory of Biorheology and Medical Ultrasonics, University of Montréal Hospital Research Centre (CRCHUM), 2099 Alexandre de Sève (Room Y-1619), Montréal, Québec H2L 2W5, Canada*

[2]*Department of Radiology, Radio-Oncology and Nuclear Medicine, and Institute of Biomedical Engineering, University of Montréal, Montréal, Québec H3T 1J4, Canada*

(Received 13 May 2008; revised manuscript received 17 September 2008; published 19 December 2008)

A Monte Carlo study on ultrasound backscattering by red blood cells (RBCs) is presented for three-dimensional (3D) distributions of particles. The cells were treated as classical spherical particles and accordingly, the Boltzmann distribution was considered to describe probability distribution of energy states of a system composed of such particles. The well-known Metropolis algorithm can generate configurations according to that probability distribution and therefore, was employed in this study to simulate some realizations of both nonaggregating and aggregating RBCs. The study of nonaggregating particles was motivated to compare simulations with existing experimental results and consequently, to validate the model. In the case of aggregating RBCs, the interaction potential between cells was modeled with the Morse potential and the frequency-dependent backscattering coefficient (BSC) was investigated at different hematocrits (H, particle volume fractions). The impact of aggregation potential on the spectral slope (SS) was also evaluated. It is shown that BSC increased as the magnitude of aggregating potential was raised and the effect was more pronounced at higher hematocrits. Moreover, spectral slopes at nonaggregating and low aggregating conditions were found to be around 4, which is consistent with the Rayleigh scattering theory. However, it had diminished significantly, particularly at higher hematocrits as the magnitude of the attractive potential energy was raised. For instance, at $H=40\%$ SS dropped from 4.04 for nonaggregating particles to 3.62 at the highest aggregating potential considered in this study. Our results suggest that this 3D model is capable of reflecting the effects of RBC aggregation on BSC and SS.

DOI: 10.1103/PhysRevE.78.061919 PACS number(s): 87.10.Rt

I. INTRODUCTION

Red blood cells in normal blood flowing through human vessels constitute reversible aggregates. Aggregates usually form rouleaux or complex three-dimensional structures [1]. The size distribution and spatial abundance of those aggregates depend upon the flow condition and concentration as well as molecular mass of large plasma proteins (macromolecules) in blood, such as fibrinogen [2,3]. The aggregation phenomenon in human blood is normal, however, hyperaggregation is a pathological state. An enhanced level of red blood cell (RBC) aggregation changes rheological properties of blood and may hamper normal circulatory functions, i.e., transportation of oxygen, nutrients, and metabolic wastes. Any deviation from normal condition can contribute to various diseases, namely, deep venous thrombosis, atherosclerosis, microcirculatory flow disorders in pathologies such as diabetes mellitus, etc. [4–6].

It is believed that the ultrasound blood characterization (UBC) technique has the potential to provide a method for *in vivo* and *in situ* evaluation of RBC aggregation and may become a diagnostic tool because the level of aggregation is directly related to the echogenicity of blood. It may be mentioned here that ultrasound waves propagating through blood are scattered as they encounter inhomogeneities in acoustic impedance. RBCs are the main scatterers of blood because their acoustic properties are different with respect to the surrounding plasma and also because they are much more numerous than any other blood cells (approximately 98% of blood particles are erythrocytes). For such systems, it is not straightforward to develop a theoretical model depicting their ultrasound scattering behaviors. This is because the scattered field is governed by complex interactions of the incident wave with a collection of suspended particles in plasma at a volume fraction (hematocrit) that may typically vary between 20 and 60% (the normal hematocrit is close to 40%). However, as RBCs are acoustically considered as weak scatterers (impedance mismatch with respect to plasma $\approx 13\%$), then multiple scattering can be neglected and accordingly, the expression of the scattered intensity can easily be cast in terms of the single-particle scattering cross section, number density of particles, and structure factor of the medium [7].

Recently, Yu and Cloutier [8] developed a modified version of this model by approximating the structure factor and used that to analyze *in vitro* experimental data to determine two physically relevant parameters of RBC clustering, the packing factor, and mean fractal diameter of aggregates. It is expected that by properly compensating biological tissue attenuation [9], this approach may allow quantitative and reproducible *in vivo* characterization of RBC aggregation. Apart from these, a large number of *in vitro* investigating protocols were also designed to observe ultrasound backscattering from blood as well as to study how it varies with shear rate, flow turbulence, hematocrit, stroke rate of pulsatile flow, and concentration of aggregating macromolecules [10–15].

*ratank.saha@crchum.qc.ca
†guy.cloutier@umontreal.ca

Besides *in vitro* and a few qualitative *in vivo* investigations on RBC aggregation, simulation studies have recently been proposed to better understand mechanisms of ultrasound backscattering by various distributions of red blood cells. Simulations enable one to vary different physical parameters in a controlled way and consequently, to examine their influence on variations of observables. Fontaine *et al.* [16] investigated backscattering by three-dimensional distributions of noninteracting cells and obtained convincing results. However, they did not consider aggregating RBCs as well as the fact that particles could not overlap due to their impenetrability. Other earlier studies based on particle dynamics or statistical mechanics examining nonaggregating or aggregating cells were mostly restricted to one or two dimensions [17–20]. Therefore, to provide a framework to interpret experimental observations, it is relevant to simulate three-dimensional distributions of nonoverlapping particles and study corresponding frequency-dependent backscattering for both nonaggregating and aggregating RBCs.

The purpose of this paper is to describe a model implementing statistical mechanics that is capable of generating three-dimensional configurations for both nonaggregating and aggregating blood samples. The nonaggregating distributions were generated by throwing particles randomly in space with the restriction that they could not overlap. For aggregating particles, configurations were produced by allowing impenetrable particles to interact attractively with neighbors. The Morse potential was used for this case to mimic the interaction pair potential. For both simulation conditions, frequency-dependent backscattering coefficients (BSCs) were computed for a wide range (7.5–200 MHz) of frequencies and associated spectral slopes were determined within a particular frequency range (up to 40 MHz) at different hematocrits. The spectral slope (SS) is an often used index in ultrasound tissue characterization that describes BSC as a function of frequency on a log-log scale. For nonaggregating RBCs, the SS is generally found to be around 4 confirming particles behave as Rayleigh-type scatterers; that is, scattered intensity depends on the fourth power of frequency. It was observed [7,12,13] that the SS remained close to that value for blood medium containing aggregates with a size smaller than $\lambda/10$. Here, λ is the wavelength of the incident wave. Essentially the numerical value of the SS diminishes as the frequency of incident wave or the size of RBC clusters increases.

The organization of the paper is as follows: We present the theoretical background in Sec. II. Simulation methods and results are elaborated on in Secs. III and IV, respectively. Section V is for discussions of our results. Here we compare our findings with earlier observations in brief as well as highlight the computational intensiveness of this work. Finally, we summarize our conclusions and the scope of future works in Sec. VI.

II. THEORETICAL BACKGROUND

A. Ultrasonic scattering by blood

1. Single-particle scattering

The angle-dependent scattering cross section can be obtained in various ways for an isolated homogeneous scatterer.

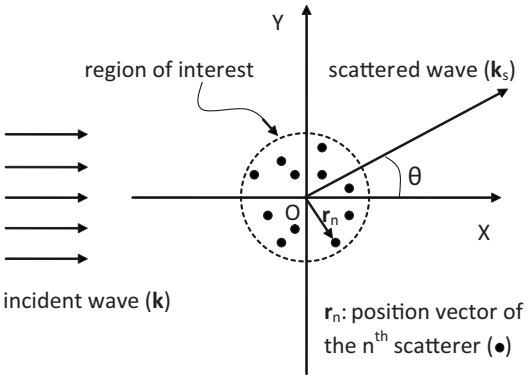

FIG. 1. Top view of the scattering diagram. Here, $\theta=\pi$, gives backscattering.

For example, exact analytical expressions of scattering cross sections exist for regular (sphere, cylinder) homogeneous scatterers [21]. On the other hand, one can also rely on approximate results of scattering cross sections because they are, in general, simple and valid even for irregular scattering objects [22]. Approximate expressions of scattering cross sections are generally obtained by solving the integral equation for pressure wave by using the Green's function method and also by approximating the acoustic field inside the scatterer in various ways [23]. In the case of the most popular Born approximation, the unknown internal field within the scatterer is assumed to be given by the incident field and accordingly, the expression for scattering amplitude can be derived. This approximation works well when the size of the scatterer is small ($kR<1$) and contrasts in acoustic properties are also small ($<\pm 15\%$), with respect to the suspending medium. Here, k is the magnitude of the incident wave vector $\vec{k}$ and R represents the radius of an equivalent sphere having the volume of a RBC. The backscattering cross section, which is of particular interest in many situations since measurements are generally carried out in the backward direction, in the Born approximation for a homogeneous spherical scatterer is given by [21,22]

$$\sigma_b(-2\vec{k}) = \frac{1}{16\pi^2}V_s^2k^4\left(\frac{(\kappa_e-\kappa)}{\kappa}-\frac{(\rho_e-\rho)}{\rho_e}\right)^2 \times\left(3\frac{\sin 2kR-2kR\cos(2kR)}{(2kR)^3}\right)^2, \quad (1)$$

where κ and ρ indicate the adiabatic compressibility and density of the surrounding medium, respectively. The same quantities for the scatterer are given by κ_e and ρ_e. The subscript b is used to denote backscattering. Here, V_s represents the volume of the spherical scatterer prototype. The scattering diagram corresponding to Eq. (1) is shown in Fig. 1.

2. Many-particle scattering

For a monodisperse medium such as blood (a dispersion of single-type scatterers), the differential backscattering cross section per unit volume (also known as the backscattering coefficient), which is defined as the scattered power per unit solid angle in the backscattering direction far away from

the scatterers divided by the intensity of the incident wave, can be cast as [24]

$$\chi_b(-2\vec{k}) = m\left\langle \frac{1}{N}\left|\sum_{n=1}^{N} e^{i2\vec{k}\cdot\vec{r}_n}\right|^2\right\rangle \sigma_b(-2\vec{k})$$
$$= mS(-2\vec{k})\sigma_b(-2\vec{k}), \quad (2)$$

where m is the number density of scatterers that is related with the hematocrit (H) as, $m=H/V_s$. Here, $S(-2\vec{k})$ is the structure factor of the insonified medium. Its ensemble average is here denoted by the symbol $\langle\ \rangle$. The position vector $\vec{r}_n$ defines the center of the nth spherical scatterer in space, as shown in Fig. 1, where N is the number of scatterers in the region of interest. In this study, Eq. (2) was evaluated for various distributions of RBCs corresponding to nonaggregating as well as aggregating conditions. This equation thus constitutes the framework of our simulations.

The structure factor in Eq. (2) represents the spatial organization of particles and for a collection of cells distributed in space, we showed earlier in the context of ultrasonic scattering by red blood cells that it can also be described by

$$S(-2\vec{k}) = \left\langle N\left|\int N(\vec{r})\exp(i2\vec{k}\cdot\vec{r})d\vec{r}\right|^2\right\rangle. \quad (3)$$

Here, $N(\vec{r})$ is the microscopic density function and for discrete scatterers, it is given by

$$N(\vec{r}) = \frac{1}{N}\sum_{n=1}^{N}\delta(\vec{r}-\vec{r}_n), \quad (4)$$

where δ is the Dirac delta function. Hence, from Eq. (3) it is clear that the structure factor can be computed by taking the Fourier transform of the microscopic density function. Therefore, by using Eq. (4) for a particular number density (m), the frequency-dependent backscattering coefficient [Eq. (2)] can be computed in the Born approximation.

Another simple variant of BSC, which is given by [25,26]

$$\chi_b(-2\vec{k}) = mW\sigma_b(-2\vec{k}), \quad (5)$$

can also be widely found in the literature. This particular form of the BSC can be derived by approximating the structure factor in the low frequency limit. For hard spherical particles, the packing factor (W), known as the Percus-Yevick packing factor, is related with the hematocrit as [25]

$$W = \frac{(1-H)^4}{(1+2H)^2}. \quad (6)$$

The BSC as expressed by Eq. (5) can be used at low frequencies (Rayleigh scattering conditions). In this paper, we use the Percus-Yevick packing theory (later abbreviated as PYPT) to refer to BSC computed with Eq. (5).

B. Interparticle interaction

One of the important determining factors of the BSC for a collection of particles is the spatial organization of corpuscles, as defined by $S(-2\vec{k})$. For human blood, which is a fluid densely packed by RBCs ($\approx$5 million RBCs per mm^3), organization of cells is governed by the resultant interparticle interaction potential originating from various force fields. For example, steric potential does not allow RBCs to overlap because although deformable, they are impenetrable in nature. Negatively charged thin layers (glycocalyx) attached with surfaces of RBCs create a screened electrostatic repulsive potential between them since they are immersed in an ionic solution. In the case of blood in motion, shear forces also have an impact on RBC interactions. Low shear conditions favor RBC collisions and aggregation, whereas RBC aggregates are disrupted at high shears. The shear dependence of RBC aggregation is reversible as shear forces are modified.

There are two mutually contradictory models to explain attractive potential between RBCs, which leads to aggregation of cells. In one model, RBC adhesion is due to the adsorption of macromolecules at the cell surface, which bridges RBCs to form stacklike structures. According to the other model, a depletion mechanism is responsible for RBC adhesion. In this case, macromolecules are rejected from the interspace between two RBCs and therefore a concentration gradient of macromolecules binds RBCs by producing an osmotic pressure near their surfaces to from rouleaux. The resultant of these potentials (steric, electrostatic, shear, adsorption or depletion) determines the magnitude and spatial extent of the RBC-RBC pair potential [1–3].

1. Pair potential for nonaggregating particles

For nonaggregating cells, the attractive potential is no longer active. The electrostatic potential can also be ignored in this case because it remains nonzero only when the surface-to-surface distance between two cells lies within few nanometers. The effect of steric potential can be written as

$$U_{ij}^{nonag} = \infty, \quad \text{if } |\vec{h}| < 2R$$
$$= 0, \quad \text{if } |\vec{h}| \geq 2R, \quad (7)$$

where h represents center-to-center separation distance between two RBCs. The pair potential was modeled as very high when the cells overlapped, otherwise it was set to zero. The superscript *nonag* denotes the nonaggregating case and the subscript ij stands for ith and jth particles.

2. Pair potential for aggregating particles

Neu and Meiselman [27] obtained an analytical form for pair potential of aggregating blood particles by considering electrostatic and depletion interactions. The validity of the model was also established by showing good matching between theoretical predictions and experimental results. However, the derivation as well as interpretation of such mathematical expressions is nontrivial. Alternatively, the Morse potential was used to represent RBC-RBC interaction energy per unit area profile [28,29], as given by

$$\phi^m(r_{ss}) = D\{\exp[2\beta(r_0 - r_{ss})] - 2\exp[\beta(r_0 - r_{ss})]\}. \quad (8)$$

In the above equation, the superscript m refers to the Morse potential. Here, r_{ss} is the surface-to-surface distance between

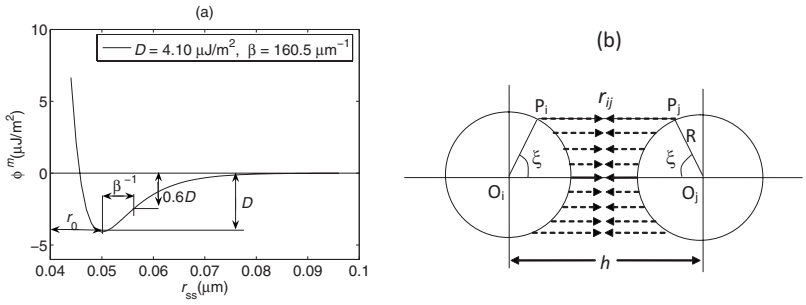

FIG. 2. (a) Typical variation of the Morse potential with surface to surface distance. The potential reaches its minimum value D at a separation distance r_0. It becomes 60% of D at a distance β^{-1} from r_0. (b) Top view of two interacting RBCs. The interaction potential acts over the surfaces exposed to each other. The dashed arrows represent the attraction between particles.

two interacting objects and r_0 is the distance where the potential reaches to its minimum value D, as shown in Fig. 2(a). Physically D can be related with the concentration of macromolecules in plasma and hence its increase results in higher RBC-RBC bond strength. The parameter β controls the width of the potential. It has a direct correspondence with the molecular size of macromolecules in practice [27–29] and determines the RBC-RBC bond length. The potential behaves as a repulsive one up to certain distances, otherwise it is attractive in nature. Further, it vanishes when separation between particles becomes much larger than the width of the potential. It was used in this study to model aggregation.

For two spherical objects as approximated for neighboring RBCs in this study, the total potential energy can be obtained by integrating the Morse potential over the interacting surface area such as

$$U_{ij}^{agg} = \int_0^{\pi/2} 2\pi R^2 \sin(\xi) D\{\exp[2\beta(r_0 - r_{ij})] - 2\exp[\beta(r_0 - r_{ij})]\}d\xi, \tag{9}$$

where $r_{ij}=h-2R\cos\xi$ is the surface-to-surface distance between the points P_i and P_j, as shown in Fig. 2(b). The superscript agg represents the aggregating case. The above integration can be worked out analytically to yield

$$U_{ij}^{agg} = \frac{\pi RD}{\beta}\{\exp[2\beta(R + r_0 - h)]\sinh(2\beta R) - 4\exp[\beta(R + r_0 - h)]\sinh(\beta R)\}. \tag{10}$$

The interaction potential between the ith and jth RBCs was therefore obtained by evaluating the right-hand side of the above expression.

3. Distribution of energy states

The total energy of the system in terms of pair potentials can be cast as

$$E = \begin{cases} \sum_{i<j} U_{ij}^{nonag} & \text{(for nonaggregating cells)} \\ \sum_{i<j} U_{ij}^{agg} & \text{(for aggregating cells)}. \end{cases} \tag{11}$$

Each pair was considered once in order to calculate the total energy. Since in this paper RBCs are treated as identical, distinguishable, and classical particles (i.e., that they follow classical mechanics and not quantum mechanics), the probability distribution of energy states (each energy state corresponds to one or more than one configuration) is given by the Boltzmann distribution [30]

$$p(E) = \frac{1}{Z}\exp(-E/k_BT). \tag{12}$$

Here, k_B, T, and Z are the Boltzmann constant, absolute temperature, and the partition function of the system, respectively. It is evident from Eq. (12) that lower energy states are more probable than those belonging to higher energies.

Therefore, some realizations of the system were generated according to their Boltzmann probability by employing the Metropolis algorithm [31]. The ensemble average of the structure factor was determined from its values at those states as

$$S(-2\vec{k}) = \sum_l S(-2\vec{k}, E_l)p(E_l), \tag{13}$$

where the subscript l denotes a state having an energy E_l. The mean structure factor was computed, in this simulation study, to obtain frequency-dependent backscattering coefficients and associated spectral slopes for three-dimensional distributions of nonaggregating as well as aggregating particles.

III. METHODS

The simulation study begins with the specification of the size of the volume to be investigated that was fixed to 70^3 μm^3. The lengths of the edges were selected as a tradeoff between the size of the computational domain and time. The computational time almost exponentially varies with the number of particles, which is determined by the size of the region of interest and by the hematocrit [19]. We shall show that even for this size we could reproduce consistent results that could be compared with those available in the literature.

The entire volume was divided into 64^3 voxels to define exactly the positions of RBCs. Therefore, particles could have only integer coordinates and structure factor could easily be determined using those coordinates. These also allowed us to generate a 3D matrix, which essentially contained pair interaction energies of a particle located at the center of the matrix with other particles that would be situated at different grid points. We computed it at the beginning of the code and stored it to use as a lookup table for future assessments. The size of the 3D matrix was 13^3, which was fixed on the basis of the spatial extent of potentials and resolution of grids. By using the lookup table during random

shuffling of the system, interaction energies of a particle could easily be determined just by knowing the coordinates of neighbors with respect to those of the particle at two configurations (initial and proposed). Interaction energies at those realizations are needed to obtain the total energy change of the system due to the trial move. Clearly, the advantage of this method was that after the generation of the lookup table, we did not require one to compute potential energy for any neighbor and also for any move during the whole process. One also should not worry that the spatial discretization scheme would introduce regularity on particle positioning. The entire volume was divided with a sufficiently large number of grids and after that, positions (grid points) were generated in random fashion such that each point was equally probable. Hence it did not introduce any regularity.

Erythrocytes were considered as identical rigid spheres with a volume V_s of 87 μm^3 and accordingly, the radius of each corpuscle was fixed to 2.75 μm [12]. The initial distribution of cells was generated by throwing them randomly in voxels and consequently, the total energy of that configuration, given by Eq. (11), was computed by summing pair potentials for periodic boundary conditions. Then, one particle was picked randomly and thrown into a new position, which was also randomly chosen. After that, the Metropolis algorithm was employed to decide whether the move had to be accepted or rejected [31]. This algorithm compared total energies [computed with Eq. (11)] between two configurations. If the energy difference (ΔE = total energy of finalconfiguration − total energy of initial configuration) was negative, a corresponding move was accepted. Otherwise it generated a random number between 0 and 1 and compared that number with the Metropolis ratio ($e^{-\Delta E/k_BT}$) for those states. The move was accepted only if the number was less than or equal to that ratio. For an accepted move, we renewed the position of the particle, otherwise it was left to reside in the same position. This corresponded to one Metropolis step. In this way the system was allowed to evolve and, in general, a significant number of Metropolis steps were required to reach equilibrium that was obtained when the energy of the system became zero or less than zero.

Once the equilibrium state was reached then the system was ready for structure factor measurements. Evaluation of Eq. (3) provided a 3D matrix containing values of structure factor at grid points corresponding to impinging waves with different magnitudes and directions of incidence. For example, each central orthogonal axis of the computed 3D matrix represented spectrum for the investigating waves propagating along that axis with spatial frequency range ≈ -1.44 to 1.39 μm^{-1}, where 0.045 μm^{-1} is the separation between two consecutive frequencies. A sufficiently large number of Metropolis iterations, which allowed expectation value not to vary significantly with iterations, were considered to obtain the ensemble average of the structure factor, as given in Eq. (13).

Besides the structure factor, the particle density (m) and frequency-dependent backscattering cross section (σ_b) had to be known to evaluate the BSC with Eq. (2). The particle density was computed by using the relation $m=H/V_s$, where in this study H was varied from 0 to 40%. The hematocrit is normally measured in practice by microcentrifugation, so it is a variable that can be easily obtained experimentally. The single-particle backscattering cross section, as given by Eq. (1), was determined by considering $\rho_e=1.092$ g/cm^3, $\kappa_e=34.1\times10^{-12}$ cm^2/dyne, whereas the same quantities for the ambient medium (blood plasma) were chosen as $\rho=1.005$ g/cm^3 and $\kappa=44.3\times10^{-12}$ cm^2/dyne, respectively [11].

IV. RESULTS

A. Nonaggregating case

Nonaggregating RBCs can physiologically occur at high flow shear rates. It can also be produced by replacing plasma by isotonic saline, as done in many experimental studies [10,11,26]. To mimic nonaggregating cells, we considered the nature of the potential as given in Eq. (7) and therefore a large repulsive potential of 10^6k_BT was assigned to each overlapping pair of RBCs.

A typical plot of the frequency-dependent simulated BSC (χ_{b0}) is shown in Fig. 3(a) for nonaggregating RBCs at frequencies between 10 and 200 MHz ($k=0.042-0.838$ μm^{-1}) and 40% hematocrit. The variation of the theoretical estimation (PYPT) that is only valid for nonaggregating cells is also shown for comparison. The two other plots (χ_{b1},χ_{b2}) are for aggregating RBCs and they are discussed later. Note that χ_{b0} has slightly higher values than the Percus-Yevick theory at each frequency and differences become more distinguishable at the highest frequencies where PYPT is no longer valid (non-Rayleigh scattering).

Note that the variation of BSC with frequency is linear on this log-log scale up to approximately 40 MHz. Therefore, the magnitude of BSC (χ_0) at a particular frequency (k_0) within that range can be extracted by performing the following power-law fitting [18]:

$$\chi_b = \chi_0(k/k_0)^s, \tag{14}$$

where the exponent s gives the slope of $\ln \chi_b$ when plotted against $\ln(k/k_0)$. As discussed earlier, that slope is termed the spectral slope (SS) in the acoustic literature. The purpose of the data fitting was to obtain BSCs at 7.5 MHz for different hematocrits in the case of nonaggregating RBCs. This was done to compare simulation results with experimental data of the literature that were obtained at that frequency. In Fig. 3(b), the solid line shows the prediction by the hard sphere Percus-Yevick packing theory. The triangles indicate experimental results for stationary saline suspensions of human RBCs reproduced from [11]. Simulated BSCs at 7.5 MHz are shown by circles (mean ± one standard deviation for 100 simulations).

This figure clearly shows that both PYPT and simulation results are in good agreement with experimental observations. However, the slight shift at a higher hematocrit of the measured scattering peak was attributed to random motion of cells due to flow disturbance originated from the experimental setup [11]. This explanation was later confirmed experimentally with pig RBCs suspended in saline [13] and the validity of the theory was thus confirmed, as the scattering peak was no longer at 18–20% hematocrit but at 13% hema-

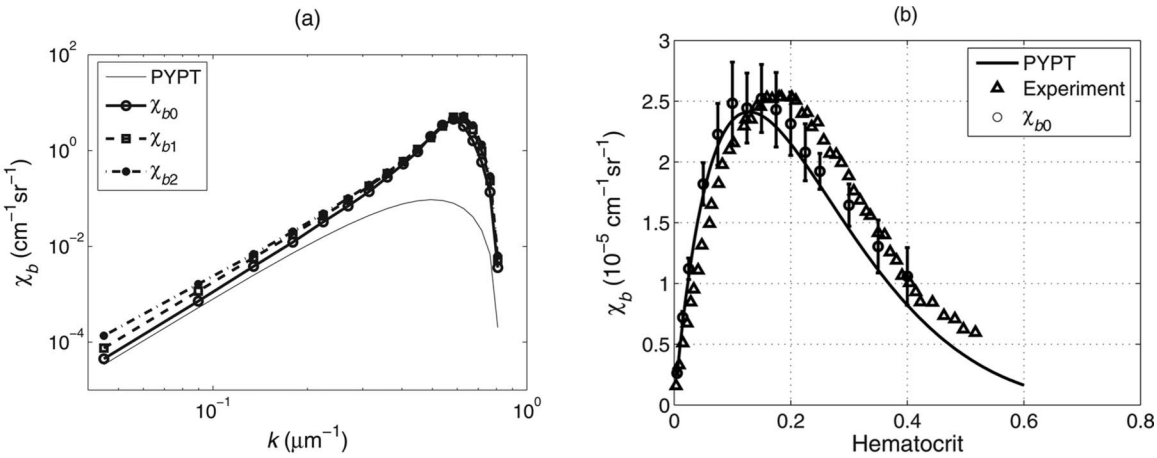

FIG. 3. (a) Frequency-dependent backscattering coefficient at a hematocrit $H=40\%$. The solid line gives the variation according to the Percus-Yevick packing theory (PYPT). Another solid line χ_{b0} represents simulation results for nonaggregating RBCs. The other two dashed lines (χ_{b1},χ_{b2}) are for aggregating bloods with $D=3.30$ μJ/m^2, $\beta=160.5$ μm^{-1} and $D=4.10$ μJ/m^2, $\beta=163.5$ μm^{-1}, respectively. RBC aggregation increases from subscripts $b0$ to $b2$. (b) Hematocrit dependence of the backscattering coefficient at 7.5 MHz for nonaggregating RBCs. The solid line (—) represents the curve for PYPT. Simulation results (χ_{b0}) are shown by the symbol ○ (mean ± one standard deviation for 100 simulations), whereas the marker △ expresses experimental results reproduced from [11].

tocrit as expected. It may also be mentioned here that the spectral slope (computed by using the first four points of the frequency-dependent BSC data [see Fig. 3(a)]) remained around 4 in the entire hematocrit range, which is consistent with the Rayleigh scattering theory (fourth-power frequency dependence).

B. Aggregating case

The Morse potential with $D=4.10$ μJ/m^2, $r_0=13.0$ nm, and $\beta=390$ μm^{-1} could give a real RBC-RBC interaction energy profile in the presence of 70 kDa dextran (dextran is a neutral polymer that can reproduce the binding effect of plasma proteins) [27]. Hence, according to this study, the interaction energy per unit area remains nonzero only when two surfaces lie within a few nanometers. This suggests that the computational domain has to be discretized in nanometric scale to simulate systems close to real blood. However, spatial discretization at this level is not possible because computational time would then become highly intensive. In the current study, r_0 was fixed to 50 nm and β was varied from 160.5 to 170.5 μm^{-1}. Moreover, the amplitude of the Morse potential D was taken in the range from 0.50 to 4.10 μJ/m^2 because for 70 kDa dextran it varied in this range at different concentrations [27]. These choices of parameters not only provided some interactions between neighboring voxels considered here but also kept computational time within practical limit. Pair potential energy was computed by using Eq. (11). Furthermore, 37 °C was chosen as the temperature of the system when evaluating the Boltzmann probability of various states.

The frequency-dependent backscattering is shown in Fig. 3(a) for aggregating blood at $H=40\%$. Two dashed lines (χ_{b1},χ_{b2}) are for aggregating cells with $D=3.30$ μJ/m^2, $\beta=160.5$ μm^{-1} and $D=4.10$ μJ/m^2, $\beta=163.5$ μm^{-1}, respectively. It is distinctively clear from the figure that enhanced levels of backscattering can be achieved by increasing the magnitude of the aggregating potential. As that magnitude was increased, spatial distribution of particles became more organized. That in turn reduced destructive interferences of scattered waves compared to nonaggregating conditions (random orientations), which resulted in higher levels of BSCs. This effect was more important at the highest aggregation potential, which is also clear from this figure. Further, higher values of BSCs also led to diminution of the spectral slopes [see the trends in Fig. 3(a) and Fig. 5].

The effect of attractive potentials on the BSC at 7.5 MHz is captured in Fig. 4(a) for fixed $\beta=160.5$ μm^{-1} and different values of D. The BSC at 7.5 MHz was determined as before, i.e., by following the same linear fitting technique as we did for nonaggregating RBCs. In Fig. 4(a), the variation of the mean BSC [normalized by the corresponding mean BSC for nonaggregating blood (χ_{b0})] for 100 simulations is presented as a function of potential depth. It reveals that the BSC increases with D and at each potential its relative increment becomes larger for higher hematocrits. For instance, at $D=3.65$ μJ/m^2, BSC was about 5.0 dB higher than χ_{b0} at $H=40\%$, whereas it was close to 1.0 dB at $H=20\%$. BSCs at 30 MHz are also shown in panel (b) of this figure to illustrate frequency-dependent behavior. It is evident that the nature of variations is similar to that at 7.5 MHz for different hematocrits. Nevertheless, at a specific potential and constant hematocrit, the rate of change of the BSC decreased as the frequency of the incident wave was increased. The reason behind this is that the spectral slopes are different in nonaggregating and aggregating bloods [see Fig. 3(a)]. The variation of the SS with aggregation potential is given in Fig. 5(a) for three different hematocrits. Note that the SS decreases at $H=40\%$ with the increase of depth D of the interaction potential. However, no clear variations of the SS are observed at $H=20\%$ and 30%, probably because of the low levels of aggregation for these cases.

The aggregation potential can also be varied by controlling the molecular weight of macromolecules, which in turn changes the depletion layer thickness in the blood suspen-

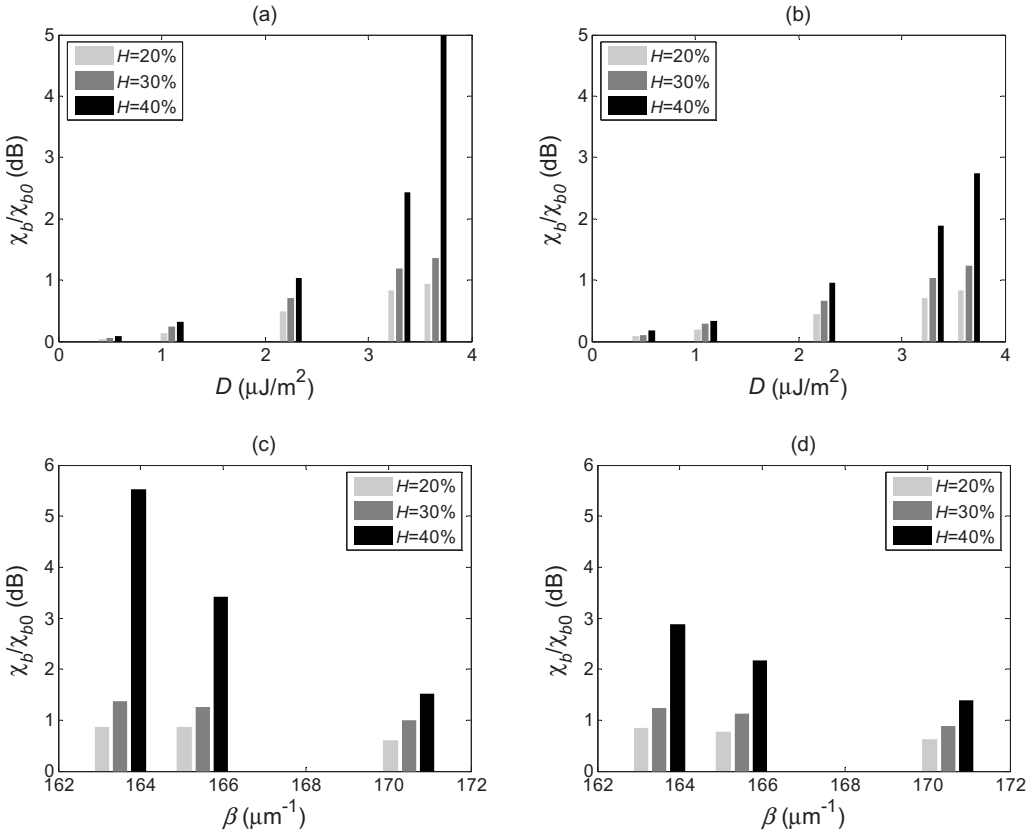

FIG. 4. (a) The effect of D on the mean backscattering coefficients at three hematocrits are shown in dB with respect to their nonaggregating cases at 7.5 MHz at fixed $\beta=160.5\ \mu m^{-1}$. (b) Same as (a) but for 30 MHz. (c) The effect of β on the mean backscattering coefficients at three hematocrits are shown when $D=4.1\ \mu J/m^2$. (d) Same as (c) but for 30 MHz.

sion. The width of the depletion region is inversely proportional to β, therefore the magnitude of the aggregation potential decreases as β increases and vice versa. A look at Fig. 4(c) gives a flavor of the influence of β on the BSC and shows that it decreases as β increases at any given hematocrit (for 100 simulations). The variation was more prominent for denser suspension. BSCs at 30 MHz also followed similar trends as at 7.5 MHz, as shown in panel (d). Figure 5(b) demonstrates how β affects the spectral slopes at different hematocrits. Here again, the impact of β on the reduction of the SS is only observed at a hematocrit of 40%.

V. DISCUSSIONS

A. Nonaggregating case

The results obtained by this simulation study revealed that they were in good agreement with those of experiments [11]. This matching also validated the numerical code developed for this purpose. It was observed that the number of iterations required to determine converging results exponentially increased with the number of particles and thus at higher hematocrits computations became more intensive. For example, at $H=0.5\%$ it was found that 20 Metropolis steps

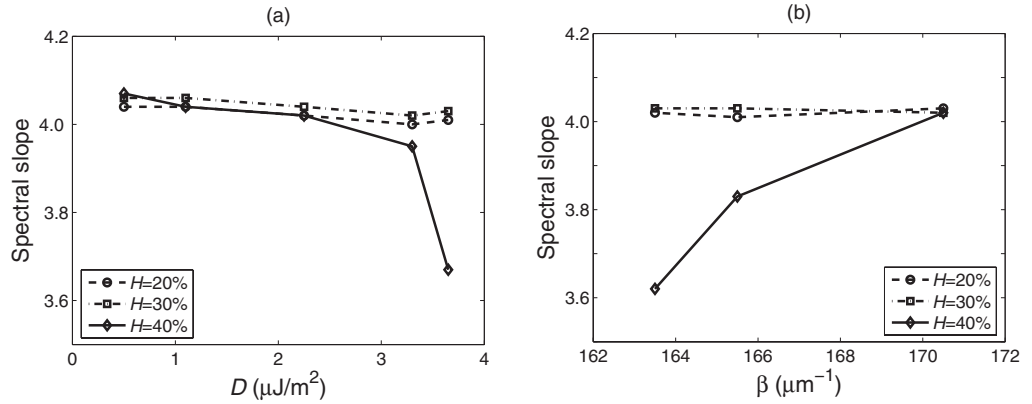

FIG. 5. (a) Variations of the spectral slope at different hematocrits with D but at a constant $\beta=160.5\ \mu m^{-1}$. (b) Same as (a) but here D remains constant at $4.10\ \mu J/m^2$ and β varies.

were sufficient to reach equilibrium and 6000 steps were good enough to obtain the ensemble average of the structure factor. It took approximately 6 min for each simulation in a node part of a computer cluster (specifications—Pentium 4: 3.2 GHz; RAM: 2 GB; operating system: RedHat Enterprise Linux 4). In contrast, those numbers were 15 and 30 million, respectively, for $H=40\%$ even for the relatively small volume of interest considered in these simulations. Corresponding execution time was around 1 h and 7 min on the same computer platform.

B. Aggregating case

In this study, we found that the BSC increased with aggregating potential and that it also caused the SS to reduce when aggregation was sufficient. Further, we observed that enhancement of the BSC at lower frequency was more than that at higher frequency for aggregating corpuscles. These findings are consistent with some earlier studies [18,32,33]. However, our numerical values, in general, are on the lower side compared to them [18,32,33]. For example, Foster *et al.* [32] measured that the BSC dropped by ≈ 14.3 dB at 35 MHz when the shear rate was raised from 3 s^{-1} to 100 s^{-1}, and also the SS decreased from 3.5 to 0.4 due to the diminution of shear rate from 32 s^{-1} to 0.16 s^{-1}. Whereas, we found at 40% hematocrit that the BSC increased by 5.5 dB at 7.5 MHz for the highest aggregation potential considered here, and the corresponding SS decreased from 4.04 to 3.62. It is expected that further enhancement of the BSC and the reduction of SS would have been possible by increasing the magnitude of the aggregation potential. However, as the interaction pair potential increased, the number of energy states of the system also increased, and therefore more iterations were required to obtain converging results at each hematocrit. For example, at $H=40\%$, for each simulation a total of 65 million iterations (execution time ≈ 4 h and 30 min) were employed when $D=1.10$ $\mu J/m^2$ but for $D=3.65$ $\mu J/m^2$ the number was 515 million and hence it required a long time (about 35 h and 46 min) to execute. In both cases β was 160.5 μm^{-1}. That is why in this paper we preferred to examine the model under low aggregation domains to obtain results within practical computational time.

It is interesting to note that the relative increase of the BSC (with respect to nonaggregating blood at the same hematocrit) is more for higher hematocrit at a constant aggregating potential (see Fig. 4). Shung *et al.* [14] also made a similar observation. They measured that the relative increase of the BSC at $H=40\%$ or $H=30\%$ was more than that of $H=20\%$. The reason behind this might be that the possibility of interactions between particles increases at higher hematocrit and also they can easily interact with each other even for low aggregating potentials. The interaction potential in turn brings more particles close to each other at higher hematocrits due to the dense network of cells and favors to form aggregates. As a result of that, destructive interferences of scattered waves are reduced more at higher hematocrits than those at lower hematocrits and thus backscattering increases more at these cases.

VI. CONCLUSIONS

A Monte Carlo study on ultrasound backscattering by red blood cells was discussed in this paper. The particles were distributed in three-dimensional space and considered as weak scatterers. Some realizations of such a system were generated by employing the Metropolis algorithm. The frequency-dependent backscattering coefficients and associated spectral slopes were determined for those configurations. The simulation results were also compared with experimental observations. For nonaggregating particles, the pair potential was defined in such a way that it would not allow particles to overlap. However, for aggregating cases, the Morse potential was used to model the interaction pair potential profile. This study enabled us to assess the influence of aggregation potential on the frequency-dependent backscattering coefficient and the spectral slope at different particle concentrations.

The main findings are that simulation results and theoretical predictions were in good agreement with experiments for nonaggregating particles. On the other hand, for aggregating cells it was demonstrated that the BSC increased as the magnitude of the attractive potential energy was raised. This effect became more prominent at higher hematocrits, i.e., at $H=40\%$ or $H=30\%$ in comparison to $H=20\%$. Furthermore, the spectral slope also decreased as the magnitude of the attractive potential attended higher values, but this was only confirmed at $H=40\%$. It would be relevant in future studies to consider bigger regions of interest to investigate larger clustering of RBCs and impacts on backscattering. This may provide a better framework to match experimental findings but at the detriment of computational load. Some studies can be carried out in the future to employ the structure factor model to analyze backscattering data from simulated three-dimensional volumes containing RBC clusters to extract information related to the packing factor and mean size of RBC aggregates [8,9]. That study may be useful to investigate how the packing factor and mean aggregate size are correlated with hematocrit. These are not clear so far. This study may put some light on the possibility of *in vivo* determination of hematocrit by the ultrasound backscattering technique. The accuracy of the model in determining the size of aggregates also needs to be validated at different physiological hematocrits. This may be another important project for future work.

ACKNOWLEDGMENTS

This work was supported by joint funding from the National Institutes of Health of the USA (Grant No. RO1HL078655), the Canadian Institutes of Health Research (Grant Nos. CMI 72323 and MOP 84358) and the Heart and Stroke Foundation of Canada (Grant No. PG-05-0313). We are grateful to the "Réseau Québécois de Calcul de Haute performance" (RQCHP) for their generous allocation of computer resources. The authors would also like to thank François T. H. Yu and Marie-Hélène Roy Cardinal of the Laboratory of Biorheology and Medical Ultrasonics (LBMU), Marianne Fenech, formerly from LBMU and now with the University of Ottawa, and Keshav Dasgupta of McGill University for their constant cooperation, support, and encouragement during this work.

[1] D. M. Surgenor, *The Red Blood Cell* (Academic Press, New York, 1975).
[2] H. Bäumler, B. Neu, E. Donath, and H. Kiesewetter, Biorheology **36**, 439 (1999).
[3] X. D. Weng, G. Cloutier, R. Beaulieu, and G. O. Roederer, Am. J. Physiol. **271**, H2346 (1996).
[4] A. Chabanel, M. H. Horellou, J. Conard, and M. M. Samama, Br. J. Haematol. **88**, 174 (1994).
[5] F. J. Neumann, H. A. Katus, E. Hoberg, P. Roebruck, M. Braun, H. M. Haupt, H. Yillmanns, and W. Kübler, Br. Heart J. **66**, 425 (1991).
[6] C. Le. Dévéhat, M. Vimeux, G. Bondoux, and T. Khodabandehlou, Int. Angiol **9**, 11 (1990).
[7] K. K. Shung and G. A. Thieme, *Ultrasound Scattering in Biological Tissues* (CRC Press, Boca Raton, 1993).
[8] F. T. H. Yu and G. Cloutier, J. Acoust. Soc. Am. **122**, 645 (2007).
[9] E. Franceschini, F. T. H. Yu, and G. Cloutier, J. Acoust. Soc. Am. **123**, EL85 (2008).
[10] G. Cloutier and Z. Qin, Biorheology **34**, 443 (1997).
[11] K. K. Shung, Y. W. Yuan, D. Y. Fei, and J. M. Tarbell, J. Acoust. Soc. Am. **75**, 1265 (1984).
[12] Y. W. Yuan and K. K. Shung, J. Acoust. Soc. Am. **84**, 1195 (1988).
[13] Y. W. Yuan and K. K. Shung, J. Acoust. Soc. Am. **84**, 52 (1988).
[14] K. K. Shung, G. Cloutier, and C. C. Lim, IEEE Trans. Biomed. Eng. **39**, 462 (1992).
[15] L. C. Nguyen, F. T. H. Yu, and G. Cloutier, Ultrasound Med. Biol. **34**, 664 (2008).
[16] I. Fontaine, M. Bertrand, and G. Cloutier, Biophys. J. **77**, 2387 (1999).
[17] I. Fontaine, D. Savery, and G. Cloutier, Biophys. J. **82**, 1696 (2002).
[18] D. Savery and G. Cloutier, IEEE Trans. Ultrason. Ferroelectr. Freq. Control **52**, 94 (2005).
[19] J. W. Hunt, A. E. Worthington, and A. T. Kerr, Ultrasound Med. Biol. **21**, 329 (1995).
[20] J. Zhang, J. L. Rose, and K. K. Shung, Ultrasound Med. Biol. **20**, 903 (1994).
[21] P. M. Morse and K. U. Ingard, *Theoretical Acoustics* (Princeton University Press, Princeton, NJ, 1968).
[22] C. C. Coussios, J. Acoust. Soc. Am. **112**, 906 (2002).
[23] S. K. Sharma and R. K. Saha, Waves Random Media **14**, 525 (2004).
[24] V. Twersky, J. Acoust. Soc. Am. **64**, 1710 (1978).
[25] V. Twersky, J. Acoust. Soc. Am. **81**, 1609 (1987).
[26] K. K. Shung, IEEE Trans. Sonics Ultrason. **29**, 327 (1982).
[27] B. Neu and H. J. Meiselman, Biophys. J. **83**, 2482 (2002).
[28] Y. Liu and W. K. Liu, J. Comput. Phys. **220**, 139 (2006).
[29] Y. Liu, L. Zhang, X. Wang, and W. K. Liu, Int. J. Numer. Methods Fluids **46**, 1237 (2004).
[30] R. K. Pathria, *Statistical Mechanics* (Butterworth-Heinemann, Oxford, U.K., 1996).
[31] N. Metropolis, A. Rosenbluth, R. Rosenbluth, A. Teller, and E. Teller, J. Chem. Phys. **21**, 1087 (1953).
[32] F. S. Foster, H. Obara, T. Bloomfield, L. K. Ryan, and G. R. Lockwood, Proc.-IEEE Ultrason. Symp. **3**, 1599 (1994).
[33] G. Cloutier, M. Daronat, D. Savéry, D. Garcia, L. G. Durand, and F. S. Foster, J. Acoust. Soc. Am. **116**, 566 (2004).